Supplementary Information for Table-top EUV Grazing-Reflection Ptychography with Full-Pose Self-Calibration

Yanqi Chen[1,2†], Hao Xu[3†], Qingxin Wang[1,2†], Yanwei Li[9†], Lei Huang[1,2,3], Zhengkang Xu[1,3], Su Li[1,2], Dongliang Wang[4,5], Yaqi Wu[7,8], Jianjie Li[9], Fei Wang[10], Xiaoshi Zhang[11,12], Bowen Liu[7,8], Guoqing Chang[4,5,6], Jie Li[1,3], Changjun Ke[3], Yishi Shi[1,2,*], Zhongwei Fan[1]

[1] School of Optoelectronics, University of Chinese Academy of Sciences, Beijing, 100190, Beijing, China.

[2]Center for Materials Science and Optoelectronics Engineering, Chinese Academy of Sciences,Beijing, 100190, Beijing, China.

[3]Aerospace Information Research Institute, Chinese Academy of Sciences,Beijing, 100190, Beijing, China.

[4]Beijing National Laboratory for Condensed Matter Physics, Institute of Physics, Chinese Academy of Sciences, Beijing, 100190, Beijing, China.

[5] School of Physics, Chinese Academy of Sciences, Beijing, 100190, Beijing, China.

[6] Songshan Lake Materials Laboratory, Dongguan, 523808, Guangdong Province, China.

[7] Ultrafast Laser Laboratory, Key Laboratory of Opto-Electronic Information Science and Technology of Ministry of Education, School of Precision Instruments and Opto-Electronics Engineering, Tianjin University, Tianjin, 300072, Tianjin, China.

[8] Georgia Tech Shenzhen Institute, Tianjin University, Shenzhen, 518071, Guangdong Province, China.

[9] Jihua Laboratory, Foshan, 518071, Guangdong Province, China.

[10]Wangzhijiang Innovation Center for Laser, Aerospace Laser Technology and System Department, Shanghai Institute of Optics and Fine Mechanics, Chinese Academy of Sciences,Shanghai, 201800, Shanghai, China.

[11]Southwest United Graduate School, Yunnan University, Kunming, 650500, Yunnan, China.
[12]School of Physics and Astronomy, Yunnan University, Kunming, 650500, Yunnan, China.
*Corresponding Author.

†These authors contributed equally to this work.

S1 Superiority of feature domain loss evaluation

In Traditional PIE algorithms evaluate errors based on raw data metrics, enforcing element-wise minimization of the difference between predictions and observations. However, when the digital forward model mismatches the actual physical process generating the observations, PIE often fails. Instead, we employ a feature-domain (FD) loss evaluation. Its general form is [1]:

$$\mathcal{L}_{fd} = \sum_{j=1}^{N} \langle \boldsymbol{\omega} \mathbf{y}_j^{\rho}, \boldsymbol{\omega} \tilde{\mathbf{y}}_j^{\rho} \rangle \tag{S1}$$

where $\boldsymbol{\omega}$ is a differentiable feature extraction operator, ρ is the scale factor and $\langle \cdot, \cdot \rangle$ denotes a function measuring distance between two variables. Amplitude-based PIE algorithms can be regarded as a special case where $\boldsymbol{\omega} = \mathbf{I}$, $\rho = 0.5$ and squared L_2 norm is used. In most cases, amplitude-based PIE is superior to intensity-based PIE with $\rho = 1$.

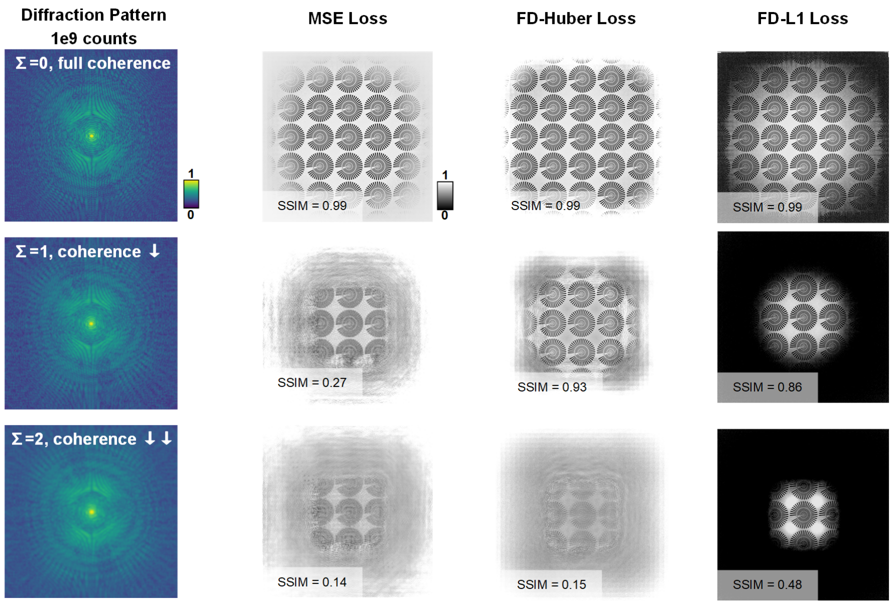

Fig. S1 Simulation results under 10^7 probe counts using different loss functions.

In point-to-point imaging systems such as FPM, real-space observations resemble natural images. Edge information ($\nabla \mathbf{y}$) is commonly employed because it directly relates to the sample's spatial distribution while remaining insensitive to illumination variations. The L_1 norm serves as the distance metric, aligning with the sparsity assumption of natural image features. As an alternative, the Huber norm addresses limitations of both L_2 and L_1 losses: it avoids the exploding gradient issue of L_2

loss in high-error regions while resolving the convergence instability from the non-differentiability of L_1 loss. This norm combines L_1 and L_2 components through a piecewise definition[2]:

$$\|\mathbf{x}\|_{Huber} = \sum_{i=1}^{n} \begin{cases} \frac{1}{2}x_i^2 & \text{for } |x_i| \leq \beta \\ \beta\,|x_i| - \frac{1}{2}\beta^2 & \text{for } |x_i| > \beta \end{cases} \tag{S2}$$

Due to the reciprocal-space nature of diffraction measurements, edge information ($\nabla\mathbf{y}$) in diffraction patterns lacks the intuitive sparsity observed in natural images. To elucidate the efficacy of gradient-domain loss in coherent diffraction ptychography, we first conduct transmission ptychography simulations at $\lambda = 17.9$ nm wavelength. The simulation configuration features pinhole illumination positioned 0.5 mm upstream of the sample with 15 μm pinhole diameter. A 10×10 scan grid with 3 μm step size is employed. We evaluate reconstruction performance using mean squared error (MSE) and feature-domain (FD) losses with L_1 and Huber norms under varying conditions of mixed Gaussian-Poisson noise (Gaussian standard deviation $\sigma = 1.5$) and decoherence, where decoherence is modeled by convolving fully coherent diffraction patterns with Gaussian kernels of standard deviation Σ[3].

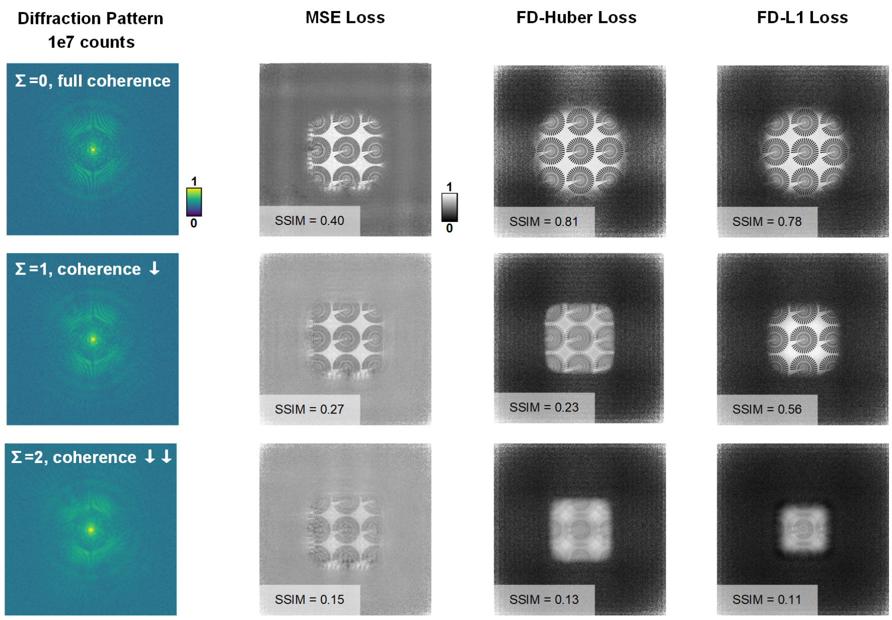

Fig. S2 Simulation results under 10^7 probe counts using different loss functions.

All loss functions are minimized using the Adam optimizer. Fig. S1 shows results under probe photon counts $= 10^9$, where the first column displays representative diffraction patterns (logarithmic scale) for $\Sigma = 0$, 1, and 2. The increasing blur in diffraction patterns reflects progressive coherence reduction, while the right three columns show reconstructed amplitude images. Reconstruction quality in the central image region is quantified using the structural similarity index measure (SSIM). Under full coherence ($\Sigma = 0$), all three losses yield comparable quality. At $\Sigma = 1$, MSE results exhibit significant degradation while both feature-domain (FD) losses maintain consistent quality, though FD-Huber marginally outperforms FD-L_1. When Σ increases to 3, only FD-L_1 successfully reconstructs the image. We further conduct simulations under low-dose illumination (10^7 probe counts) in Fig. S2. Here, MSE loss produces blurred reconstructions even under full coherence ($\Sigma = 0$), whereas FD-Huber and FD-L_1 losses retrieve high-contrast images by effectively utilizing high-frequency diffraction pattern information despite low SNR. Note that FD-Huber achieves slightly higher SSIM than FD-L_1 at $\Sigma = 0$. At $\Sigma = 1$, only FD-L_1 succeeds, while all methods fail at $\Sigma = 2$.

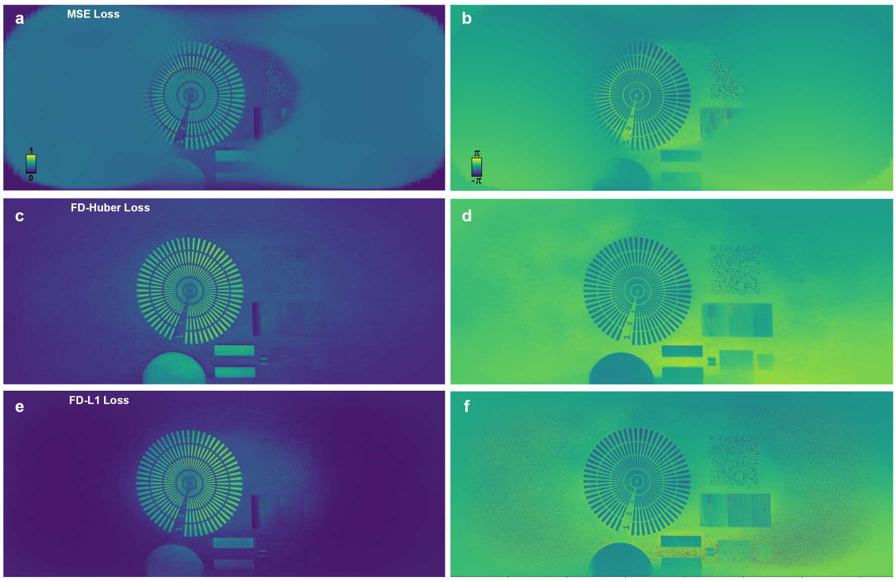

Fig. S3 Experiment results using different loss functions. **a** and **b** are amplitude and phase images using MSE, **c** and **d** are amplitude and phase images using FD-Huber and **e** and **f** are amplitude and phase images using FD-L1

Simulation results validate the efficacy of feature-domain (FD) loss evaluation, demonstrating significant robustness against model mismatch from noise and coherence degradation. This inversely indicates that edge information in diffraction patterns constitutes a stable feature, maintaining invariance under model deterioration. Specifically, we conclude that FD-Huber loss is optimal for moderate model degradation, while FD-L_1 loss withstands more extreme degradation. This justifies employing FD-Huber loss in our EUV experiments where light source coherence and flux degradation exist but remain moderate. Experimental results for the Siemens star sample (Fig. S3), reconstructed using corrected system parameters, reveal that MSE loss confines the effective field of view (FOV) to the central region, whereas FD losses achieve clear full-FOV imaging. Compared to FD-Huber, FD-L_1 yields noisier reconstructions with weaker peripheral features. Overall, FD-Huber loss demonstrates superior compatibility with our experimental conditions.

S2 Impact of incorrect parameter on reflection ptychography reconstruction

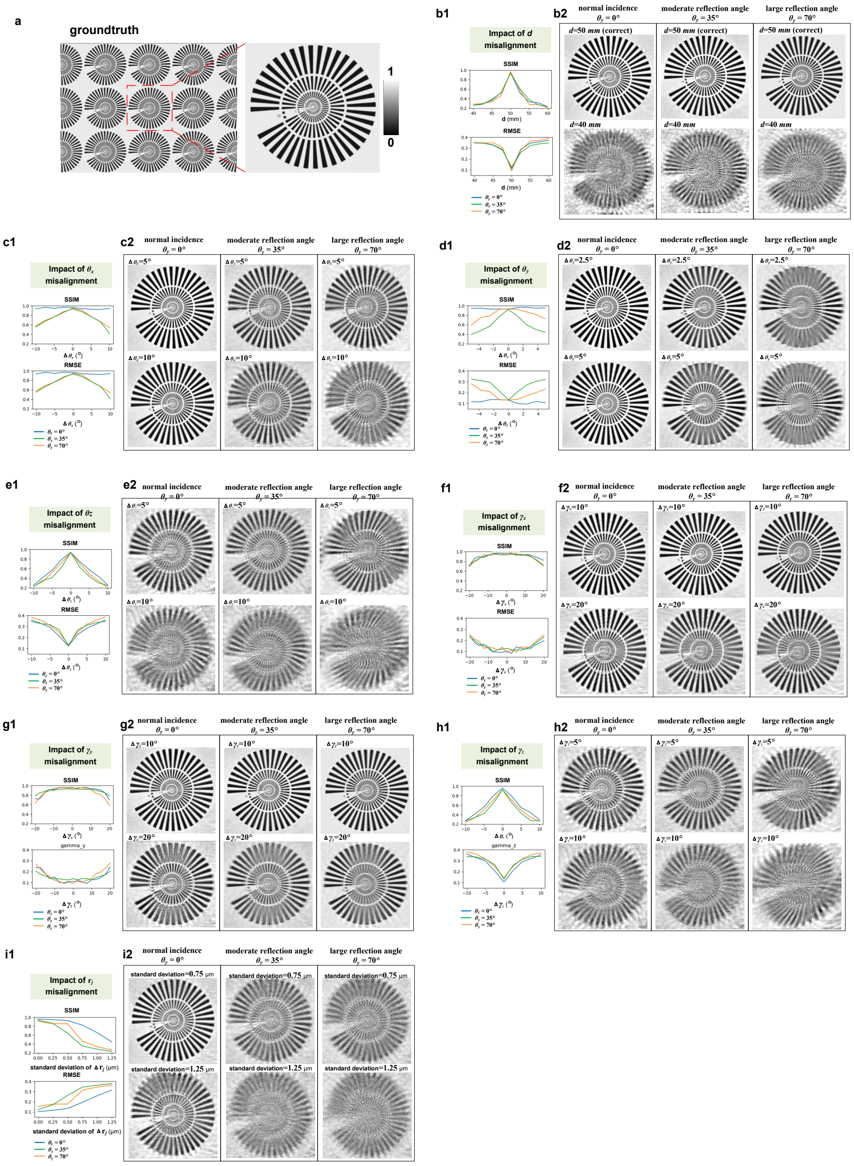

Fig. S4 Simulation of the impact of an incorrect parameter on the reflection ptychography reconstruction. **a** is the amplitude ground truth of the sample. **b-i** illustrate specific impact of different parameter misalignment with image quality index SSIM, RMSE and reconstructed results.

In this section, we systematically investigate the impact of parameter inaccuracies on reflective ptychography reconstruction through simulations. In reflection geometry, the reflection angle is closely related to the difficulty of reconstruction. Therefore, we simulate the influence of various parameter misalignment on reconstruction quality under different reflection angles. The ground truth of the sample used in the simulations is shown in Fig. S4a. To prevent the reconstruction crosstalk between amplitude and phase from affecting the calculation of evaluation metrics, an amplitude-only object is used here. Due to the limited scanning area, we focus only on the Siemens star pattern in the central region in the subsequent analysis. Three different reflection illumination settings are considered: 0° (normal incidence), 35° (moderate reflection angle), and 70° (high reflection angle), all with a diffraction distance of 50 mm and a scanning grid of 10×20 (3 μm step size, $\sim$70% overlap ratio with 15 μm pinhole probe). The effects of different parameter misalignment are presented in terms of structural similarity index (SSIM) and root mean square error (RMSE) between the reconstructed results and the ground truth in curves Fig. S4(b1)–(i1), and the reconstructed ROIs are displayed in panels Fig. S4 (b2)–(i2).

It is noteworthy that the influence of θ_x, θ_y, and $\mathbf{\Delta r_j}$ is strongly correlated with the illumination angle setting: the larger the reflection illumination angle—that is, the closer to grazing incidence—the more severe the impact of errors in these three parameters. Conversely, under normal incidence illumination, errors in θ_x and θ_y have virtually no effect on the reconstruction results. Moreover, the individual misalignment of all parameters affects the reconstruction quality to some extent, with some parameters having a more pronounced effect under grazing incidence setting. It can therefore be further inferred that in the presence of combined parameter errors, the imaging quality will deteriorate even further. This not only explains why transmission or small-angle reflection ptychography tends to achieve better imaging quality, whereas grazing-incidence reflection ptychography generally yields poor imaging quality, but also underscores the necessity of comprehensive misalignment correction.

S3 Coupling effect among system parameters

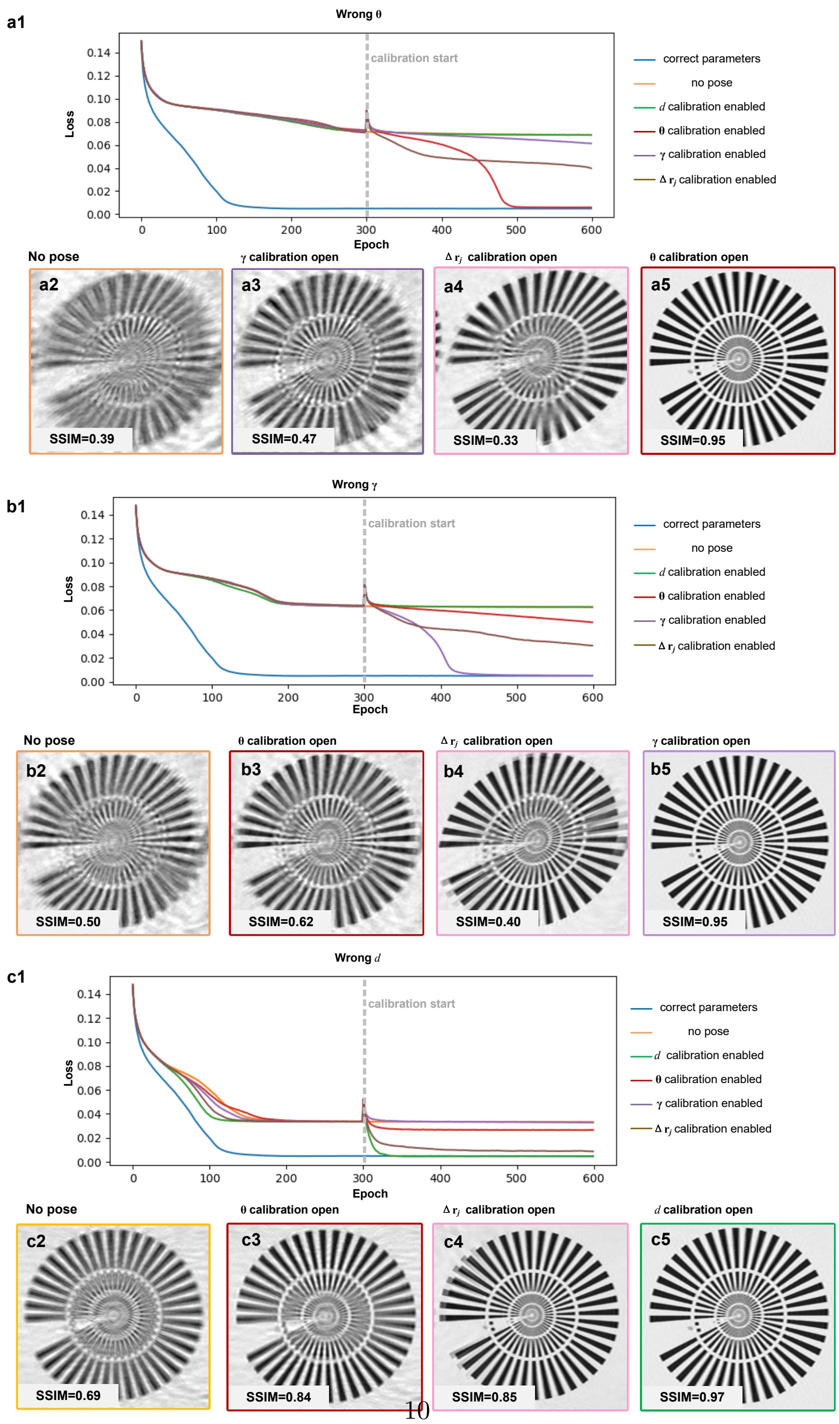

Fig. S5 Simulation test of the coupling effect among parameters. **a1** show the loss decrease curve with calibration of individual parameters enabled when $\boldsymbol{\theta}$ is incorrectly set, **a2-a5** present the reconstruction results corresponding to the curves in **a1**. **b1-b5** and **c1-c5** show the test of $\boldsymbol{\gamma}$ parameter and d parameter.

In reflection ptychography systems, different parameters may not be completely independent, meaning that errors induced by the misalignment of one parameter could potentially be compensated by adjusting another parameter. This may affect the effectiveness of self-calibration. Therefore, we investigate the coupling relationships among system parameters through simulation experiments. The parameter settings in the simulation are $d = 50$ mm, $\boldsymbol{\theta} = [0°, 70°, 0°]$ and $\boldsymbol{\gamma} = [0°, 0°, 0°]$. We deliberately mis-set one parameter (e.g., $\boldsymbol{\theta}$) and then test whether other individual parameters can compensate for the error caused by this mis-set parameter. If enabling the self-calibration of another parameter (differs from the mis-set one) leads to a decrease in the loss function, we consider that parameter coupling occurs. The test results when parameters $\boldsymbol{\theta}$, $\boldsymbol{\gamma}$, and d are mis-set are shown in Fig. S5a-c, respectively. In Fig. S5a, $\boldsymbol{\theta}$ is incorrectly set to $[5°, 72°, 5°]$. We enable the self-calibration of a single parameter at the 300th epoch. It can be observed that after enabling the self-calibration for $\boldsymbol{\gamma}$, the loss function decreases slightly, whereas after enabling self-calibration for the scanning position error, the loss function decreases significantly. This indicates that $\boldsymbol{\theta}$ exhibits different degrees of coupling with $\boldsymbol{\gamma}$ and the scanning position, while the coupling to the scanning position is stronger. However, this coupling cannot fully compensate for the error, as only when the correction for $\boldsymbol{\theta}$ itself is enabled does the loss decrease to a level consistent with reconstruction using the correct parameters. Moreover, in terms of reconstruction results, only after enabling the correction for $\boldsymbol{\theta}$ is the image distortion completely eliminated. In Fig. S5 b and c, where $\boldsymbol{\gamma}$ and d are incorrectly set to $[5°, 5°, 5°]$ and 49 mm, we observe similar phenomena: there exists relatively weak coupling among pose parameters (e.g., between d and $\boldsymbol{\theta}$), while stronger coupling exists between the scanning position and the pose parameters. Nevertheless, the best results are achieved only when the correction for the mis-set parameter itself is implemented.

Based on the above findings, we employ a segmented updating strategy for full-pose self-calibration. Specifically, in the first stage, no parameter calibration is performed, which allows the iterative process to stabilize. In the second stage, calibration of the pose parameters is enabled, and in the third stage, calibration of the scanning position is added. The main purpose of this approach is to prevent the coupling effect between pose parameters and scanning position from affecting the image reconstruction quality. We validated the effectiveness of this strategy using simulations, as shown in Fig. S6 , where the ground truth parameters are$d = 50$ mm, $\boldsymbol{\theta} = [5°, 72°, 5°]$ and $\boldsymbol{\gamma} = [5°, 5°, 5°]$ while the incorrect settings are $d = 49$ mm, $\boldsymbol{\theta} = [0°, 70°, 0°]$ and $\boldsymbol{\gamma} = [0°, 0°, 0°]$. Fig. S6 a compares the loss function decrease for reconstruction with correct parameters, the segmented updating strategy (pose parameters calibration enabled at the 200th epoch, scanning position calibration enabled at the 1400th epoch), and the simultaneous updating strategy (calibration of all parameters enabled at the 200th epoch). During the second stage, the loss decrease in the segmented strategy is slower compared to the simultaneous strategy, but in the third stage, it drops rapidly to the same level as that achieved with the correct parameters—a result not attained by the simultaneous strategy. The reconstruction results under the three scenarios are shown in Fig. S6 b, c, and e. It can be seen that the segmented strategy completely corrects the image distortion and allows the pose parameters to converge to their correct values, whereas the simultaneous strategy fails. This demonstrates the effectiveness of the proposed segmented updating strategy, which can decouple the relationship between pose parameters and the scanning position, thereby preventing the iteration from getting trapped in a local optimum.

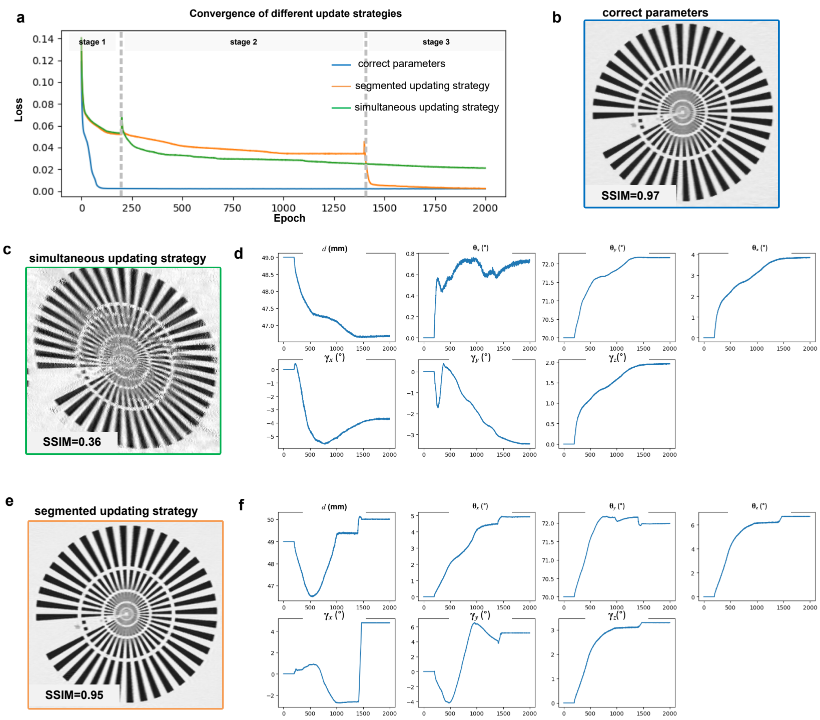

Fig. S6 Simulation validation of the proposed segmented updating strategy. **a** is the loss decrease curve of reconstruction with correct parameters, segmented updating strategy and simultaneous updating strategy. **b** is the reconstruction result with correct parameters. **c** and **d** is the reconstruction result and parameter updating curve with simultaneous updating strategy; **e** and **f** is the reconstruction result and parameter updating curve with segmented updating strategy

S4 Impact of illumination dose

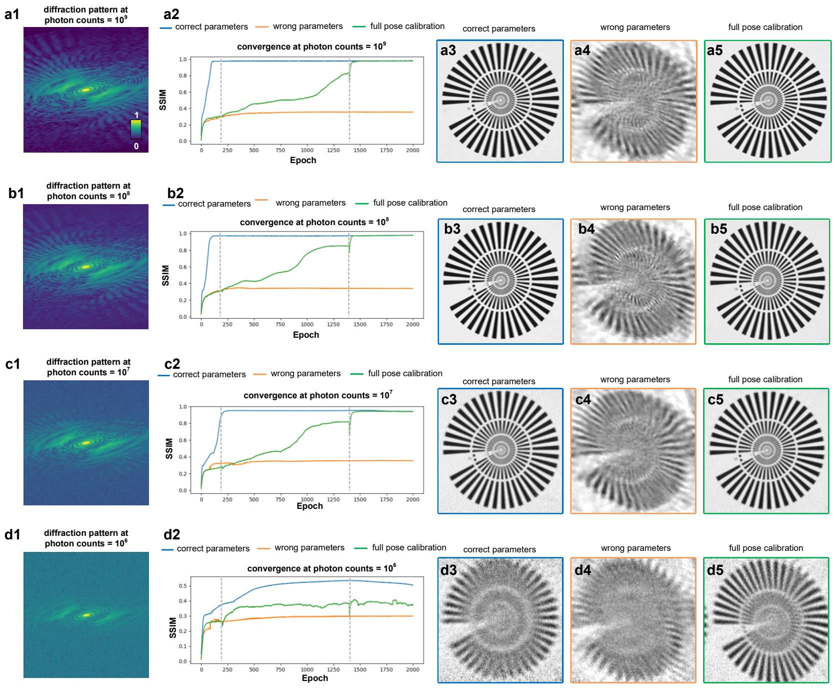

Fig. S7 Simulation test of the impact of illumination dose. **a1** illustrates one of the diffraction patterns at 10^9 photon counts, **a2** are the SSIM curves in the reconstruction with correct parameters, wrong parameters and full pose calibration, **a3-a5** are the reconstruction results corresponding to three scenarios. Similarly, **b1-b5**, **c1-c5**, **d1-d5** are the test results at 10^8, 10^7,10^6 photon counts, respectively.

In coherent diffraction imaging, the illumination dose has a significant impact on phase retrieval. To investigate the effectiveness of full-pose calibration under different dose levels, we conducted simulation experiments. The system parameters were set as in the previous section, and four different experimental conditions were defined, corresponding to probe photon counts of 10^9, 10^8, 10^7, and 10^6. The imaging results are shown in Fig. S7 a-d. In panels a2–d2, the curves of SSIM between the reconstructed image and the ground truth over epochs are plotted. We consider the calibration successful if this metric, after enabling full-pose calibration, reaches a level comparable to that achieved with the correct parameters. It is observed that only when the illumination dose drops to the level of 10^6 counts does full-pose calibration fail to improve reconstruction quality. However, at this dose level, the reconstruction quality even with the correct parameters is already much lower than at other dose levels. In real experiments, we employ high dynamic range (HDR) fusion to enhance the signal-to-noise ratio of the raw diffraction patterns. The longest exposure time used is 640 μs, corresponding to approximately 10^8 photon counts, which is sufficient to support the effective implementation of full-pose calibration.

S5 Surface topography characterization of the customized wafer sample

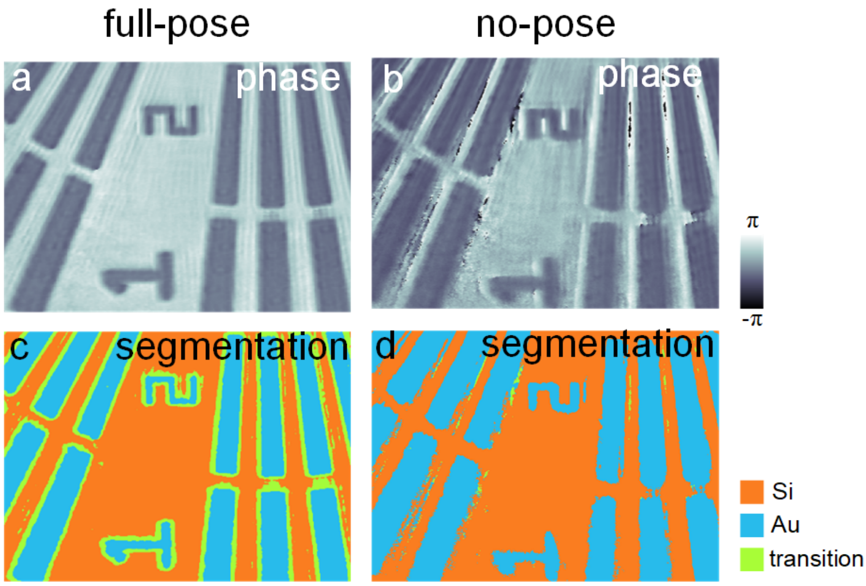

Fig. S8 Segmentation of gold structures, the silicon substrate and transition area using phase result with full-pose and no-pose self-calibration.

Based on the complex pixel values and their spatial positions, the reconstructed complex-valued object can be segmented into three distinct clusters, corresponding to the gold structures, the silicon substrate, and the transition region. To achieve precise segmentation, we employed the Gaussian Mixture Model clustering (GMMc) method[4], initialized using the k-means clustering algorithm[5], followed by 500 iterations to ensure convergence and obtain stable classification results. This procedure enables accurate determination of the phase values (Φ_{obj}) associated with the gold structures and the silicon substrate. Segmentation using phase image with and without full-pose self-calibration is shown in Fig.S8. It's seen full-pose self-calibration yields clear phase image and allows accurate determination.

The relative surface height of the sample can be derived from the phase difference between the gold structures and the silicon substrate. The measured phase values are determined by: (1) the phase shifts arising from differences in surface reflection, as described by the Fresnel relations, and (2) the accumulated phase changes due to propagation over different optical path lengths. This relationship can be expressed as $\Phi_{obj} = \Phi_r + \Phi_h$, where the first term corresponds to the reflection-induced phase shift, and the second term represents the phase accumulated during spatial propagation.

Given prior knowledge of the sample's material composition and height, we neglect the effect of multiple reflections caused by the beam passing through the structures and reflecting again. Thus, the first term is obtained by calculating the phase of the Fresnel coefficients for the relevant interfaces. The computational approach and optical constants were taken from Refs.[6] and [7], interpolated to 17.90 nm to match the experimental wavelength. Subsequent Φ_r with Full-pose and no-pose learning is -2.10 rad and -1.98 rad, respectively. For the second term, under oblique incidence at an angle $\phi_{inc} \sim= \theta_y$, the accumulated phase shift due to a structural height h can be expressed as $\Phi_h = 4\pi h \sin(\pi/2 - \phi_{inc})/\lambda$. It is noteworthy that, in our experimental conditions (wavelength of 17.90 nm, incidence angle of $\sim$70°), a designed height of 35 nm induces phase wrapping effects. Incorporating prior knowledge, we corrected the gold structure phase values by adding 4π. The surface height is finally calculated by $h = \lambda(\Phi_{obj} - \Phi_r)/[4\pi h \sin(\pi/2 - \phi_{inc})]$.

S6 Scanning electron microscope characterization of the tested samples

As a reference for the EUV reflection ptychography results, we present the images of the customized wafer sample and the chip sample observed under a Scanning Electron Microscope (SEM). Fig.S9a is a large-field image (magnified 500 times) of the customized wafer sample with b and c being the enlarged region of the Siemens star pattern and the maze pattern, while Fig S10a is the large field image (magnified 300 times) of the chip sample. Fig.S9b and c correspond to the region of interest in Fig.S44 c1 and k1, while the white dashed area in Fig.S10b corresponds to the region of interest mentioned in the Fig.S4 b, where black stains can be seen. Fig.S10c shows the details of the grating area. Through calibration, the line width of a single grating is 42.7 nm (as indicated by the red solid line), and the distance between two adjacent groups of longitudinal grating areas is 2.26 μm (as indicated by the yellow dashed line).

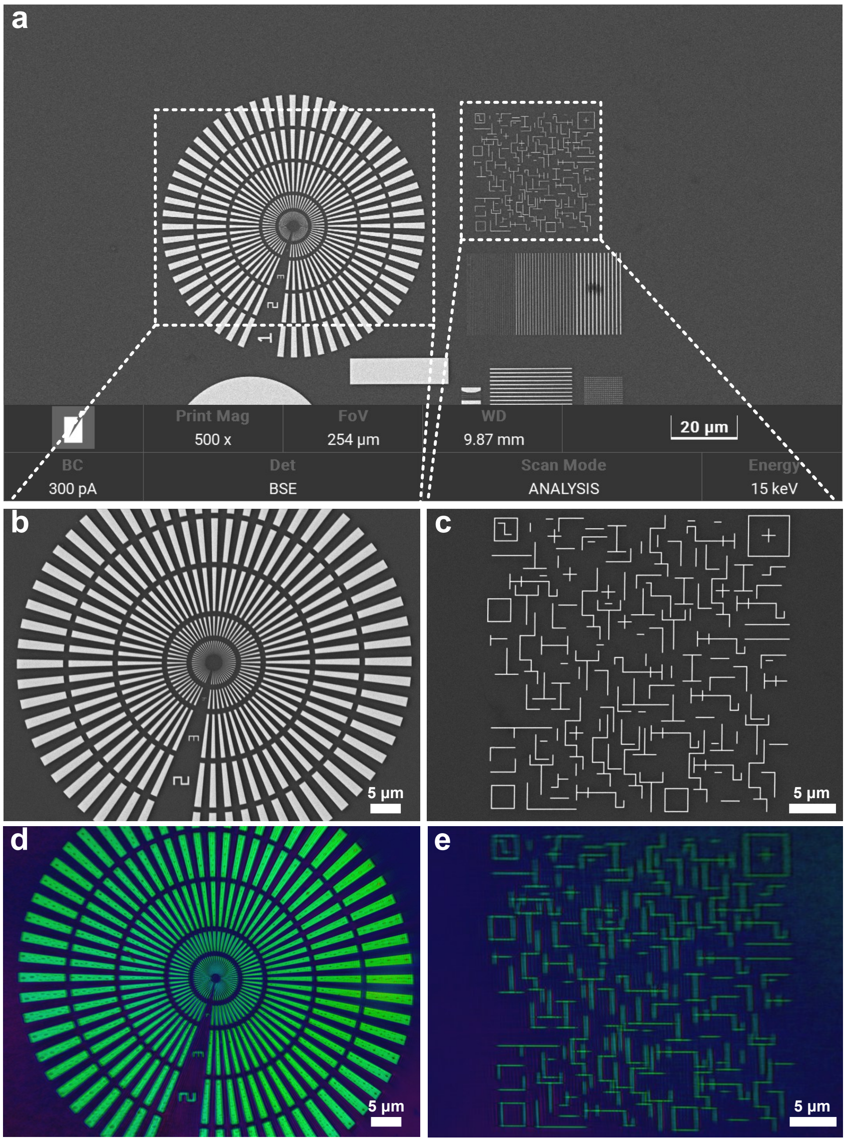

Fig. S9 SEM image of the customized wafer sample. **a** is a large-field image (magnified 500 times) of the customized wafer sample. **b** and **c** are the enlarged Siemens srar and maze pattern. **d** and **e** are the EUV ptychography images (with full-pose self-calibration) corresponding to **b** and **c**.

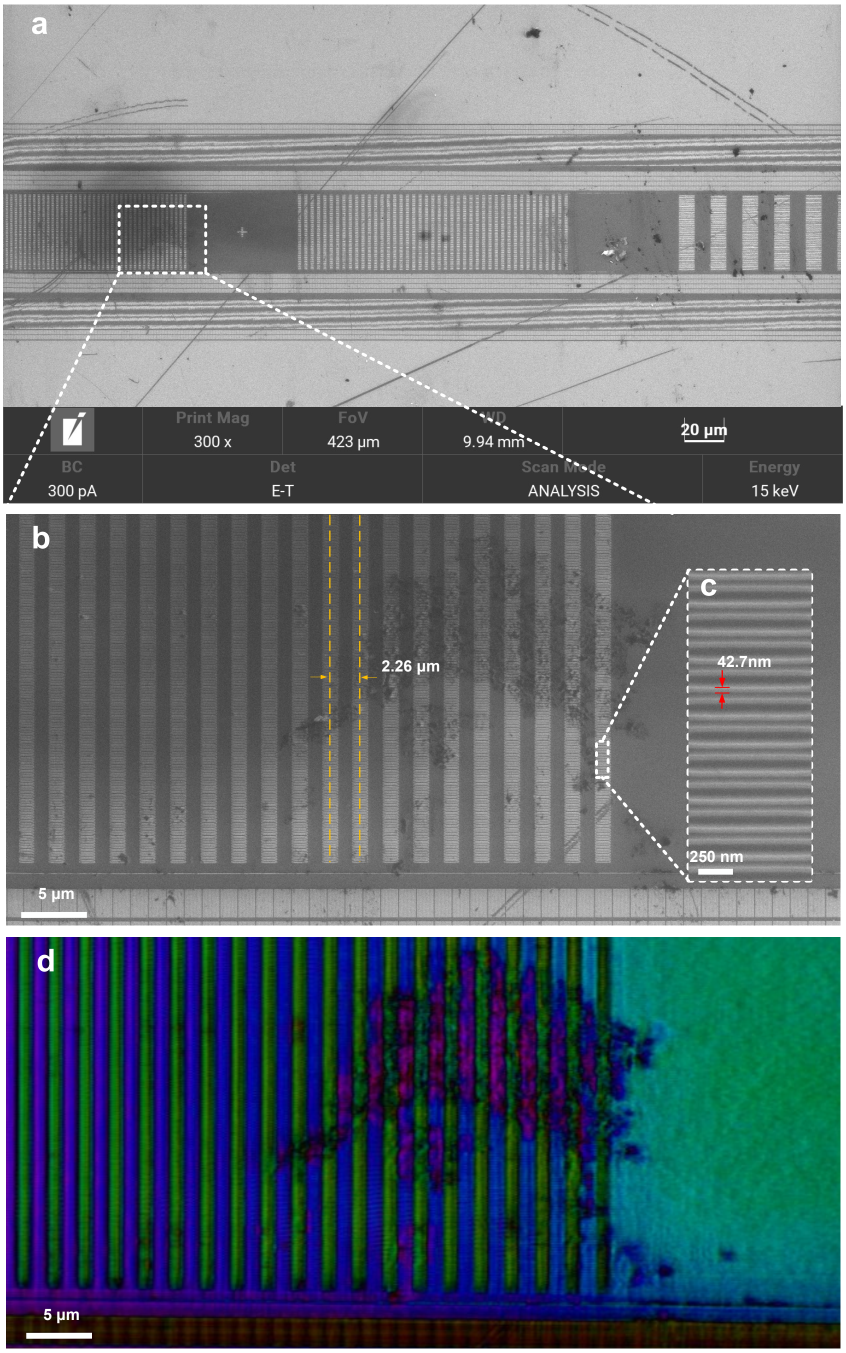

Fig. S10 SEM image of the chip sample. **a** is a large-field image (magnified 300 times) of the chip sample. **b** is the enlarged region with black stain while **c** is the enlarged grating area. **d** is the EUV ptychography image (with full-pose self-calibration) corresponding to **b**.

S7 Table-top EUV beamline at 17.9 nm

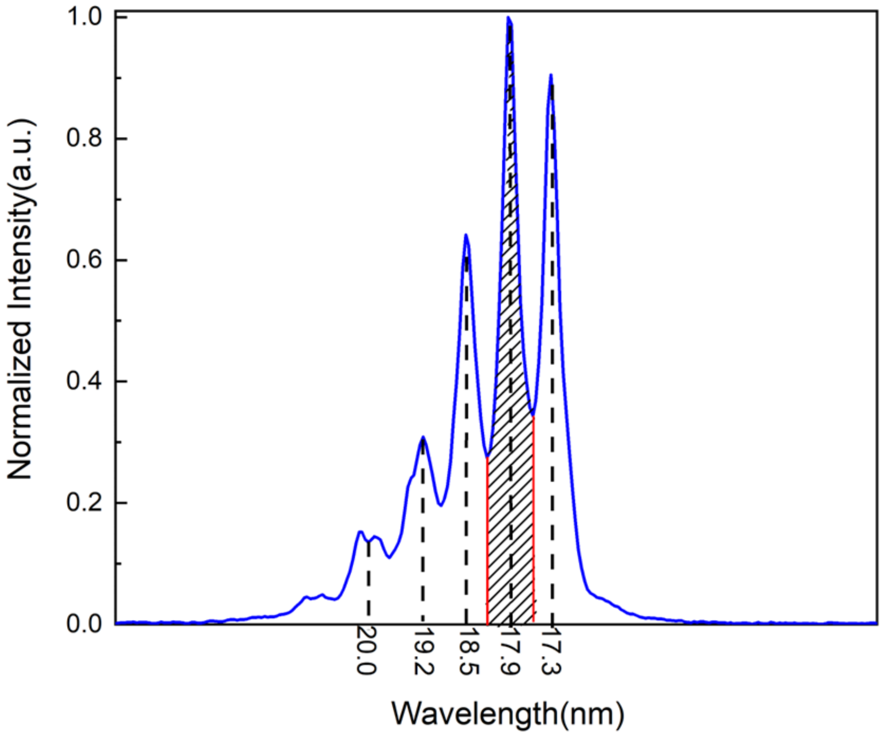

Fig. S11 Spectrum of EUV laser (before monochromatization) measured after Al film .

A femtosecond laser offers 1.1 mJ, 190 fs pulses at a central wavelength of 1036 nm and a repetition rate of 4 kHz, corresponding to 4.4 W average power. Whereafter, the pulse width is compressed to 30 fs in a hollow-core fiber system followed by the chirped mirrors. After compression, the laser with 3.34 W residual power is focused into a HHG chamber by a lens of 200 mm focal length. EUV radiation including 17.9 nm is generated in a gas cell filled with Argon (Ar) gas. A 200 nm thick aluminum (Al) film further eliminates residual driven laser. The average power of EUV laser is measured after Al film by a EUV photodiode (AXUV 100G). A home-build EUV spectrometer [**?**] reveals the spectral distribution of harmonics. Fig.S11 shows the measured spectrum of EUV laser (before monochromatization). Sharp absorption band of Al at 17 nm infers the wavelength of harmonics. Conservative estimation of 17.9 nm proportion is 20%. The average power of 17.9 nm haromnic peak is 95 nW after Al film and 0.2 μW in gas cell.

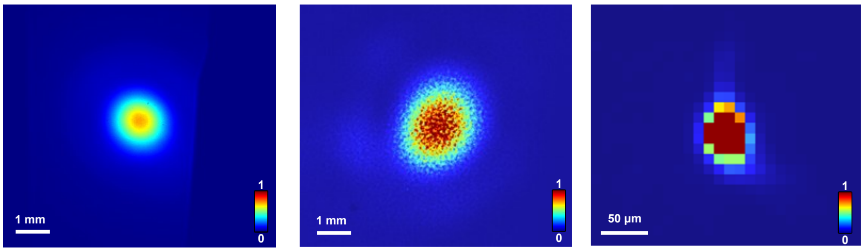

Fig. S12 **a** Multiwavelength EUV spot. **b** Monochromatic 17.9 nm spot. **c** Focused 17.9 nm spot.

Two narrowband EUV multilayer mirrors centered at 17.9 nm (optiXfab, reflection bandwidth FWHM∼600 pm, reflectance Rs > 50%) act as a monochromator and a condenser to focus the beam to the sample. Fig.S12**a** shows multiwavelength EUV beam spot filtered by Al film on a sCMOS mounted 2.3 m away from gas cell. Diameter of EUV beam here is 1.3 mm. Fig.S12**b** is a picture of monochromatic 17.9 nm EUV light after two monochromatic flat mirrors. Coarse wavefront comes from limited flatness of the mirrors. Fig.S12**c** shows focused 17.9 nm spot after one monochromatic flat mirror and one monochromatic concave mirror with a radius of curvature of 500 mm. The intensity on focus is too high that sCMOS is overexposed in an exposure time of 1 ms. The diameter of the focal spot is less than 50 μm.

References

[1] Zhang, S., Berendschot, T.T., Zhou, J.: Elfpie: an error-laxity fourier ptychographic iterative engine. Signal Processing **210**, 109088 (2023)

[2] Meyer, G.P.: An alternative probabilistic interpretation of the huber loss. In: Proceedings of the Ieee/cvf Conference on Computer Vision and Pattern Recognition, pp. 5261–5269 (2021)

[3] Lin, H., Lin, A., Jin, X., Li, K., Niu, J., Li, J., Zhang, X., Liu, T., Xu, W., Zhang, F.: Ultra-broadband ptychography for dispersive samples. Nature Communications **16**(1), 5714 (2025)

[4] A robust em clustering algorithm for gaussian mixture models. Pattern Recognition **45**(11), 3950–3961 (2012)

[5] Na, S., Xumin, L., Yong, G.: Research on k-means clustering algorithm: An improved k-means clustering algorithm. In: 2010 Third International Symposium on Intelligent Information Technology and Security Informatics, pp. 63–67 (2010)

[6] Gullikson, E.: X-Ray Interactions With Matter. https://henke.lbl.gov/optical$_{c}onstants/$

[7] Henke, B.L., Gullikson, E.M., Davis, J.C.: X-ray interactions: Photoabsorption,

scattering, transmission, and reflection at e = 50-30,000 ev, z = 1-92. Atomic Data and Nuclear Data Tables **54**(2), 181–342 (1993)